International Journal of Heat and Fluid Flow 36 (2012) 153–166

Contents lists available at SciVerse ScienceDirect

International Journal of Heat and Fluid Flow

journal homepage: www.elsevier.com/locate/ijhff

Modeling of aerated stirred tanks with shear-thinning power law liquids

R. Sungkorn [a,1], J.J. Derksen [b], J.G. Khinast [a,c,*]

[a] Institute for Process and Particle Engineering, Graz University of Technology, A-8010 Graz, Austria
[b] Chemical and Materials Engineering, University of Alberta, Edmonton, Alberta, Canada T6G 2G6
[c] Research Center Pharmaceutical Engineering, A-8010 Graz, Austria

ARTICLE INFO

Article history:
Received 7 July 2011
Received in revised form 19 January 2012
Accepted 11 April 2012
Available online 11 May 2012

Keywords:
Computational fluid dynamics
Lattice-Boltzmann method
Euler–Lagrange model
Aerated stirred tank
Non-Newtonian liquids
Bubble breakup
Bubble coalescence

ABSTRACT

Detailed simulations of aerated stirred tanks with shear-thinning power law liquids are presented. The lattice-Boltzmann scheme was used to discretize the filtered conservation equations of the liquid phase. The motion of bubbles was tracked based on the Euler–Lagrange approach with a bubble cluster concept. The collision, breakup and coalescence of bubbles were modeled as stochastic events. The predicted flow field of a single-phase stirred tank with shear-thinning power law liquid shows reasonable agreement with experimental data. For aerated systems, qualitatively similar gas holdup distribution was achieved when comparing the predicted result with experiments. Using the proposed modeling approach, it was found that a change in rheology alters the number mean diameter, Sauter diameter and the shape of bubble size distribution.

1. Introduction

Many processes in the chemical and biochemical industries involve aeration of liquids in stirred tank reactors. For example, in bioreactors oxygen is supplied to microorganisms or cell cultures via a sparger and, together with a substrate, is distributed by a turbulent liquid flow induced by an impeller. At the start of a fermentation process the rheology of the liquid phase often exhibits Newtonian behavior and gradually changes to non-Newtonian behavior during the process. Consequently, a change in rheology may cause stagnant zones, insufficient oxygen transfer and poor bulk mixing. One of the most challenging tasks is to create adequate liquid mixing and a large interfacial contact area, while avoiding shear damage of microorganisms caused by too vigorous mixing (Arlov et al., 2008; Gogate et al., 2000).

Computational fluid dynamics (CFDs) is widely perceived as a powerful method for gaining insight into the operation of such reactors. Several research groups have attempted to establish a framework for modeling of aerated stirred reactors with a Newtonian liquid. Bakker and Van den Akker (1994) used a flow field obtained from a single-phase simulation as basis to solve the conservation equations of the gas phase (i.e., one-way coupling), taking the breakup and coalescence of bubbles into account. Ranade and Van den Akker (1994) proposed a computational snapshot approach to model the suction and ejection around impeller blades. In their work, a two-fluid model was employed to describe gas–liquid flow, and the standard k–ε model was used as the closure for turbulence. The simulation predicted gas flow around the blades and the accumulation of gas behind them. Deen et al. (2002) used a sliding grid method to simulate the motion of the impeller relative to the tank wall. The predicted mean and root-mean-square liquid velocity components in the impeller region agreed well with their measured data. Lane et al. (2005) employed a multi-reference frame technique to predict a gas–liquid flow field induced by the impellers. The breakup and coalescence of bubbles were taken into consideration via a bubble number density equation. Montante et al. (2007, 2008) solved a population balance equation (PBE) with breakup and coalescence models to predict the local bubble size distribution (BSD). Zhang et al. (2008) employed an inner–outer iterative algorithm to model the fluid motion induced by the impeller blades. They concluded that large eddy simulation (LES) provided a greater accuracy than the standard k–ε model for the prediction of the mean liquid flow field and the gas holdup. In the above studies, both gas and liquid phases were treated as interpenetrating continua (Euler–Euler (EE) approach), which is preferred for the simulation of large-scale units due to its relatively low computational demand. However, it fails to offer bubble-level information, such as information regarding the interaction between bubbles and reactor components and the bubble size distribution.

* Corresponding author at: Institute for Process and Particle Engineering, Graz University of Technology, A-8010 Graz, Austria. Tel.: +43 316 873 7978; fax: +43 316 873 7963.
E-mail address: khinast@tugraz.at (J.G. Khinast).
[1] Present address: Chemical and Materials Engineering, University of Alberta, Edmonton, Alberta, Canada T6G 2G6

0142-727X/$ - see front matter © 2012 Elsevier Inc. All rights reserved.
http://dx.doi.org/10.1016/j.ijheatfluidflow.2012.04.006

Recently, with advances in computational hardware, an Euler–Lagrange (EL) approach, under which each individual bubble is treated as a single point, gained increasing popularity among researchers. Derksen (2003) employed a two-way coupled Lagrangian particle tracking (LPT) model with LES to study the suspension of solid particles in a stirred reactor. The effect of the impeller and other reactor components were modeled using an immersed boundary condition (IBC). A two-way coupled LPT model with a mono-disperse assumption and LES were used by Arlov et al. (2008) to study gas–liquid flows in an aerated stirred reactor. A volume-of-solid method was employed to model the motion of the rotating impeller. Most recently, Sungkorn et al. (2011) extended the work of Derksen (2003) by tracking the motion of bubbles, including the breakup and coalescence phenomena, using the stochastic model of Sommerfeld (2001) and Sommerfeld et al. (2003). They suggested that this was an alternative technique to simulate large-scale reactors and to numerically study the effects of operating conditions and reactor configurations.

In contrast to the modeling of aerated stirred reactors with a Newtonian liquid, references to modeling of aerated stirred reactors with a non-Newtonian liquid are rarely found in the literature. Venneker et al. (2002) studied the dispersion of gas in pseudoplastic Xanthan solutions. A single-phase flow field was scaled with the drop of power consumption to obtain a gas–liquid flow field. They termed this method a 1½-way coupling. A black-box approach was used to model the flow in the impeller region. A closure relation for the drag coefficient derived from an experiment with non-Newtonian liquid was employed. The breakup and coalescence of bubbles were taken into account via a PBE. Moilanen et al. (2006, 2007) employed an EE approach with PBE to study fermentors with pseudoplastic liquids. Several turbulence models for Reynolds-averaged Navier–Stokes (RANS) equations were tested. Typical phenomena in pseudoplastic liquids, such as cavern formation and gas-slugs, were reproduced in their simulations. The studies involving non-Newtonian liquids cited above were limited to the EE approach based on RANS models. It is well-known that time-dependent, anisotropic turbulence characteristics, which directly relate to the breakup and coalescence of bubbles, cannot be accurately captured by RANS models. Therefore, a more sophisticated modeling technique is required to correctly predict the flow field in a stirred reactor, as well as the evolution of bubbles in terms of trajectory, velocity and size.

It is the objective of this work to develop a numerical technique that contributes to establishing the framework for the modeling of complex aerated stirred tanks encountered in industries. Our approach is based on an EL approach presented by Sungkorn et al. (2011, 2012). A variation of a lattice-Boltzmann (LB) scheme by Somers (1993) (see also Eggels and Somers, 1995; Derksen and Van den Akker, 1999) was used to discretize the liquid phase conservation equations. Non-Newtonian liquid behavior according to the power-law fluid model was incorporated in the LB scheme via an *ad hoc* modification suggested by Gabbanelli et al. (2005). The effect of the impeller and other reactor components was modeled using the IBC proposed by Derksen (2003).

2. Numerical modeling

2.1. Non-Newtonian liquids

The so-called generalized Newtonian model is used in engineering practice to describe steady-state shear flows of non-Newtonian liquids (Bird et al., 2007). It simply replaces the constant viscosity with the apparent viscosity μ_{app}, which relates to the shear rate, i.e., the second invariant of the rate-of-strain tensor $\dot{\gamma} = \sqrt{S_{ij}S_{ij}}$. The simplest empirical model for μ_{app} is the power-law model expressed as $\mu_{app} = K\dot{\gamma}^{n-1}$, where K is the consistency coefficient, and n is the power-law index. $n < 1$ corresponds to shear-thinning (pseudoplastic) liquids, $n = 1$ to Newtonian liquids, and $n > 1$ to shear-thickening (dilatant) liquids. However, the power-law model may yield unphysical viscosity, e.g., a singularity occurs when the shear-thinning liquid is at rest (i.e., when $\dot{\gamma} = 0$). In order to overcome this problem, Gabbanelli et al. (2005) proposed that the liquid assumes non-Newtonian behavior only within a limited range of $\dot{\gamma}$, with a constant value outside the range. They proposed a truncated power-law model with an *ad hoc* modification as:

$$\mu_{app} = \begin{cases} K\dot{\gamma}_0^{n-1}, & \dot{\gamma} < \dot{\gamma}_0 \\ K\dot{\gamma}^{n-1}, & \dot{\gamma}_0 < \dot{\gamma} < \dot{\gamma}_\infty \\ K\dot{\gamma}_\infty^{n-1}, & \dot{\gamma} > \dot{\gamma}_\infty \end{cases}, \tag{1}$$

where $\dot{\gamma}_0$ and $\dot{\gamma}_\infty$ represent the predefined minimum and maximum shear rate, respectively. This model was adopted in our LB scheme to calculate the apparent viscosity. Based on the LB scheme, the values of $\dot{\gamma}_0$ and $\dot{\gamma}_\infty$ were estimated according to the numerical stability criteria, i.e., the kinematic apparent viscosity $\nu_{app} = \mu_{app}/\rho$. Our preliminary results suggested that the value of ν_{app} for a stable simulation was in the range between 1.0×10^{-7} and 1.0×10^{-3} (in lattice unit). For instance, $\nu_{app} = 1.0 \times 10^{-7}$ implies a shear rate of $\dot{\gamma}_\infty \approx 2.0 \times 10^5$ N, and $\nu_{app} = 1.0 \times 10^{-3}$ implies for $\dot{\gamma}_0 \approx 1.0 \times 10^{-6}$ N in all multiphase flow simulation cases in this work. The maximum shear rate to be expected in the stirred reactor (especially in the impeller region) is well below $\dot{\gamma}_\infty$. While $\dot{\gamma}_0$ has a significant effect only at the start-up of the simulation when liquid has almost no motion (resulting in a very low shear rate). Hence the (artificial) shear rate limits in Eq. (2) have only marginal effects on the flow physics.

2.2. Lattice-Boltzmann scheme

The fundamental idea of the LB scheme is to use a many-particle system governed by mass and momentum conservation laws to simulate macroscopic flows obeying the same conservation laws. A set of (fictitious) particles residing on a lattice propagates to its neighbor sites and exchanges momentum with particles coming its way. The Navier–Stokes equations (within the incompressible limit) are solved via appropriately designed collision rules and topology of the lattice.

The specific LB scheme used in this work was proposed by Somers (1993) (see also Eggels and Somers, 1995; Derksen and Van den Akker, 1999). It is based on the staggered formulation and utilizes so-called filter matrices and solution vectors with second order convergence in space and time. The scheme was chosen because of its robustness at low viscosities (high Reynolds numbers) due to its treatment of high-order terms. Particularly, it explicitly provides the information of the flow field required for the turbulence model and the generalized Newtonian model. For instance, the rate-of-strain tensor S_{ij}, can be directly obtained from the solution vector stored locally at each grid node, it does not require numerical differentiator.

2.3. Liquid phase hydrodynamics

Flow structures in a single-phase stirred reactor are known to be highly complex due to time-dependent, three-dimensional phenomena covering a wide range of spatial and temporal scales (Derksen and Van den Akker, 1999). Under typical operating conditions for low-viscosity fluids, the impeller Reynolds number Re_r, defined as $\mathrm{Re}_r = ND^2/\nu$, is in the transition ($100 < \mathrm{Re}_r < 10{,}000$) and turbulent regime ($\mathrm{Re}_r > 10{,}000$) (Hemrajani and Tatterson, 2004). During the last decades, much progress has been made in understanding and modeling of turbulence in single-phase stirred

reactors with Newtonian liquids (Sommerfeld and Decker, 2004; Murthy and Joshi, 2008; Hartmann et al., 2004). In contrast, turbulence in non-Newtonian liquids is currently considered an area of ongoing research. For example, turbulence modeling in non-Newtonian liquids is performed by using direct numerical simulations or by adopting an existing turbulence model for Newtonian liquids. Based on the concept of Reynolds number similarity, Venneker (1999) postulated that turbulence dynamics are not affected by the non-Newtonian behavior of the liquid, at least in the bulk. He further assumed that turbulent non-Newtonian flows could be treated similarly to turbulent Newtonian flows, unless a reliable turbulence model for non-Newtonian liquids is available. The complexity drastically increases when gas is dispersed into a turbulent flow. With only a moderate amount of bubbles in a system, bubbles may induce so-called pseudo-turbulence caused by their motion relative to the liquid that results in turbulent-like flow structures. Also the amount of bubbles in the system, the bubble size distribution and their properties are the important factors that affect the intensity of the pseudo-turbulence.

In this work, the evolution of large-scale motions was addressed by applying a filtering process to the conservation equations of the liquid phase, i.e., we performed Large Eddy Simulations (LES) based on the lattice-Boltzmann scheme. The effect of the residual motion for scales smaller than the filter width was modeled using the subgrid-scale (SGS) model by Smagorinsky (1963). SGS motion is considered to be purely diffusive, and the model only drains energy from the resolved motion without feedback. Based on the suggestion of Venneker (1999), the SGS viscous stress for the non-Newtonian liquids was treated in the same manner as for Newtonian liquids. It was further assumed that, within a dilute dispersion limit, the pseudo-turbulence induced by bubbles resembles the liquid phase SGS motion and can be modeled using a similar SGS model. The eddy viscosity concept represents the total effect of the SGS motion as

$$\nu_t = (C_S\Delta)^2 S, \tag{2}$$

where C_S is the Smagorinsky constant, Δ is the filter width (with size equal to the grid spacing h_σ), and $S = \sqrt{S_{ij}S_{ij}}$. The value of C_S was set to 0.10 throughout this work. Note that hereinafter liquid properties in Eqs. (1) and (2) are resolved properties, unless stated otherwise. Hence, the effective viscosity in the conservation equations, which is a summation of the apparent viscosity and the eddy viscosity ($\nu_{eff} = \nu_{app} + \nu_t$), is a function of the resolved flow field.

Since the systems under consideration have a global gas phase volume fraction of only up to 3%, it was assumed that the void fraction term in the conservation equations of the liquid phase had only a marginal effect on the flow and that the filtered conservation equations for a single-phase flow were approximately valid (Sungkorn et al., 2011, 2012; Hu and Celik, 2008). The effect of the reactor components, i.e., impeller, baffles and tank wall, on the liquid phase was modeled using an immersed boundary condition (IBC) approach, under which the forces exerted by the reactor components were included in the conservation equations via source terms (Goldstein et al., 1993; Derksen et al., 1997). From a theoretical point of view, the assumptions proposed above were conjectural. However, it is well known that, to date, no reliable and accurate model of a multiphase flow with non-Newtonian liquids is available. Additionally, as stated previously, the objective of this work is to put forward the modeling of this type of reactor using the available knowledge. Thus, the validity of the presented modeling technique was substantiated and discussed below.

2.4. Bubble dynamics

A bubble cluster concept with a point-volume assumption, under which each parcel represents a group of bubbles with an identical diameter and velocity, was employed in this work (see Sungkorn et al. (2011) and references therein for further detail). The motion of bubbles within a parcel was tracked in a Lagrangian manner by solving Newton's equation of motion, including all relevant forces, such as net gravity force $\mathbf{F}_G$, forces due to stress gradients $\mathbf{F}_S$, drag $\mathbf{F}_D$, net transverse lift $\mathbf{F}_L$ and added mass force $\mathbf{F}_A$. The following set of equations was solved:

$$d_t\mathbf{x}_p = \mathbf{u}_p, \tag{3}$$

$$\rho_p V_p d_t\mathbf{u}_p = \mathbf{F}_G + \mathbf{F}_S + \mathbf{F}_D + \mathbf{F}_L + \mathbf{F}_A, \tag{4}$$

where $\mathbf{x}_p$ is the centroid position of the parcel, $\mathbf{u}_p$ is the bubble velocity, and ρ_p is the bubble density. Expressions of the forces acting on a bubble and their coefficients are summarized in Table 1.

Table 1
Expressions for forces acting on a bubble.

Force	Closure
$\mathbf{F}_G = (\rho_p - \rho_l)\ V_p\mathbf{g}$	–
$\mathbf{F}_S = \rho_l V_p D_t\mathbf{u}$	–
$\mathbf{F}_D = -\frac{1}{2}C_D\rho_l\pi r_p^2\lvert\mathbf{u}_p - \mathbf{u}\rvert(\mathbf{u}_p - \mathbf{u})$	$C_D = \frac{16}{\mathrm{Re}_p}(1 + 0.173\mathrm{Re}_p^{0.657}) + \frac{0.413}{1 + 16300\mathrm{Re}_p^{-1.09}}$
	$C_L = \begin{cases} \min[0.288\tanh(0.121\mathrm{Re}_p), f(Eo_d)], & Eo_d < 4 \\ f(Eo_d), & 4 < Eo_d \leqslant 10 \\ -0.29, & Eo_d > 10 \end{cases}$
$\mathbf{F}_L = -C_L\rho_l V_p\ (\mathbf{u}_p - \mathbf{u}) \times \nabla \times \mathbf{u}$	$Eo_d = \frac{Eo}{E^{2/3}}, E = \frac{1}{1 + 0.163Eo^{0.757}}$
	$f(Eo_d) = 0.00105Eo_d^3 - 0.0159Eo_d^2 - 0.0204Eo_d + 0.474$
$\mathbf{F}_A = -C_A\rho_l V_p(D_t\mathbf{u}_p - D_t\mathbf{u})$	$C_A = 0.5$

The drag coefficient C_D was estimated using a correlation derived from the experimental drag curve as a function of the bubble's Reynolds number $\mathrm{Re}_p = \rho_l|\mathbf{u}_p - \mathbf{u}|^{2-n} d_p^n / K$ with ρ_l being the liquid density, u the liquid velocity at the centroid of the parcel and d_p the bubble diameter (Dewsbury et al., 1999). The Eötvös number that appeared in the correlation for the lift coefficient C_L was defined as $Eo = (\rho_l - \rho_p)|\mathbf{g}|d_p^2/\sigma$ with $\mathbf{g}$ and σ being the gravitational acceleration and the surface tension, respectively. The liquid velocity appearing in Newton's equation of motion was the resolved liquid velocity $\tilde{\mathbf{u}}$ plus the residual liquid fluctuating component $\mathbf{u}'$, i.e., $\mathbf{u} = \tilde{\mathbf{u}} + \mathbf{u}'$. The first component was interpolated from the Eulerian grid nodes, and the fluctuating component was obtained by solving a Langevin-type model due to Sommerfeld et al. (1993). The effect of bubbles (on the Lagrangian reference frame) on the liquid phase (on the Eulerian grid) and vice versa, i.e., the two-way coupling, was accounted for using fourth-order polynomial mapping functions (Deen et al., 2004). The forces exerted by the bubbles on the liquid phase were drag, lift and the added mass force.

Bubble–bubble collisions were calculated using the stochastic inter-particle collision model of Sommerfeld (2001) and Sommerfeld et al. (2003). The model describes the collision between a bubble and its fictitious collision partner generated based on the statistics stored at Eulerian grid nodes. As a result of the collision, the coalescence of the bubbles takes place when the contact time τ_{ij} is shorter than the film drainage time t_{ij}. Otherwise, a momentum exchange and bouncing of the bubbles occur. The contact time was expressed as:

$$\tau_{ij} = \frac{C_C R_{ij}}{u_n}, \tag{5}$$

with the equivalent bubble radius R_{ij}

$$R_{ij} = 2.0\left(\frac{2}{d_p} + \frac{2}{d_{fict}}\right)^{-1}, \tag{6}$$

In Eq. (6) $\mathbf{u}_n$ is the relative approaching velocity in a normal direction. The subscript *fict* represents properties of the bubbles in a fictitious parcel. C_C is the deformation distance as a fraction of the effective bubble radius set to 0.25 (Sommerfeld et al., 2003). The film drainage time was described (neglecting the effects due to surfactants and Hamaker forces) as

$$t_{ij} = \sqrt{\frac{R_{ij}^3 \rho}{16\sigma}} \ln\left(\frac{h_0}{h_f}\right). \tag{7}$$

The initial film thickness h_0 and the final film thickness before rupture h_f were assumed to be equal to that in an air–water system, i.e., 0.1 mm and 0.01 μm, respectively. A more accurate value for h_0 and h_f may be estimated from the correlations suggested by Chesters (1975, 1991) but would require much additional computational time. Properties of the bubbles after coalescence were calculated based on the mass and momentum balance. The resulting bubble diameter was calculated as $d_{p,new} = (d_{p,old}^3 + d_{fict}^3)^{1/3}$ and the number of bubbles in a parcel as $n_{p,new} = n_{p,old}(d_{p,old}/d_{p,new})^3$. It is noted that, to the authors' best knowledge, a reliable model for bubble coalescence in non-Newtonian liquids is not yet available. Therefore, we assumed that the coalescence model derived from experiments with Newtonian liquids introduced above is approximately valid for the coalescence of bubbles in non-Newtonian liquids. We justified this assumption by the favorable results shown in the next section.

Bubble breakup was assumed to be due to bubble interaction with turbulent eddies. It was further assumed that only eddies whose sizes were smaller or equal to the bubble diameter participated in the breakup mechanism. Larger eddies simply transported the bubble without causing breakup. The breakup model by Luo and Svendsen (1996) was modified to include the apparent viscosity in the estimation of micro-scale eddies (Eq. (11)) which will be used to calculate the breakup rate of a bubble in non-Newtonian liquids. The rate of breakup of a bubble with volume V_p into a bubble with a volume of $V_p f_{BV}$ and $V_p(1 - f_{BV})$ when colliding by turbulent eddies of the size ranging from $\lambda_{\min}$ to d_p was expressed by:

$$\frac{\Omega_B(V_p : V_p f_{BV})}{(1-\alpha_g) n_p} = 0.923\left(\frac{\varepsilon}{d_p^2}\right)^{1/3} \int_{\xi_{\min}}^{1} \frac{(1+\xi)^2}{\xi^{11/3}} \times \exp\left(-\frac{2 c_f \sigma}{\rho\, \varepsilon^{2/3} d_p^{5/3} \xi^{11/3}}\right) d\xi, \tag{8}$$

where α_g is the gas phase volume fraction, $\varepsilon = 2\rho v_t^3/(C_S\Delta)^4$ is the energy dissipation at the centroid of the parcel and $\xi_{\min} = \lambda_{\min}/d_p$. The breakage volume f_{BV} was randomly chosen from the U-shape distribution:

$$f_{BV} = 0.5 + 0.5 \tanh\left(10\frac{(RN - 0.5)}{\pi}\right), \tag{9}$$

where RN is a uniform random number within the interval [0,1]. The value of f_{BV} was limited to the interval [0.2,0.8]. Accordingly, the increase of surface area c_f was computed from $c_f = f_{BV}^{2/3} + (1 - f_{Bv})^{2/3} - 1$. The minimal size of the turbulent eddies $\lambda_{\min}$ was assumed to be proportional to the length of micro-scale eddies λ_{ms} as $\lambda_{\min} = 11.4\lambda_{ms}$. Instead of a constant kinematic viscosity for a Newtonian liquid, the local apparent viscosity and energy dissipation rate was used to estimate λ_{ms} as:

$$\lambda_{ms} = \left(\frac{\nu_{app}^3}{\varepsilon}\right)^{1/4}. \tag{10}$$

Bubble breakup was considered to be a stochastic event. The breakage volume randomly generated in Eq. (9) was used to calculate the breakup rate of a bubble into a new volume $V_p f_{BV}$. The success of the breakup was determined by comparing the breakup rate during the specified time interval with a uniform random number in the interval [0,1]. The number of bubbles in a parcel after the breakup was calculated similarly to how the coalescence of bubbles was calculated. To avoid unphysical consecutive breakups of the bubbles (especially in the impeller region where turbulence intensity is relatively high) and to obtain a time-step resolution–independent solution, the breakup event was bounded by the particle-eddy interaction time t_e. That is, only one group of eddies interacted with the parcel in question for the duration of the particle-eddy interaction time. The next calculation of the breakup rate was carried out after t_e (s).

3. Practical aspects of the simulations

Aerated stirred reactors as described in the work of Venneker (1999) and Venneker et al. (2002) were used to validate the present modeling technique as well as the numerical model of the reactor. The reactor had a standard configuration and consisted of a cylindrical, flat-bottomed, baffled vessel with diameters $T = 0.286$ and $T = 0.441$ m in the single- and multiphase study cases, respectively. In all cases, the liquid fill-level was equal to the reactor diameter, i.e., $H = T$. The reactor was equipped with a standard Rushton turbine with a diameter $D = T/3$ located at a distance from the bottom $C = D$. In case of aeration, a ring sparger was placed midway between the impeller and the tank bottom. The impeller Reynolds number for shear-thinning power law liquids was computed as $\mathrm{Re}_r = \rho N^{(2-n)} D^2 / K k_s^{(n-1)}$ with k_s being the Metzner–Otto constant chosen to be equal to 11 (Metzner and Otto, 1957; Grenville and Nienow, 2004). Settings of single- and multiphase simulation cases are summarized in Tables 2 and 3, respectively.

Table 2
Overview of single-phase simulation cases.

Case	N (rpm)	K (kg/m s^{2-n})	n (−)	Re$_r$ (−)	$nx \times ny \times nz$
A1	480	0.0119	0.68	2600	$88 \times 88 \times 88$
A2	480	0.0119	0.68	2600	$66 \times 66 \times 66$
A3	480	0.0119	0.68	2600	$112 \times 112 \times 112$

Table 3
Overview of multiphase simulation cases.

Case	N (rpm)	Q_g (L/s)	K (kg/m s^{2-n})	n (−)	Re$_r$ (−)
B1	300	1.0	0.0367	0.65	12,000
B2	300	–	0.0367	0.65	12,000
B3	300	1.0	0.0010	1.00	112,000
B4	300	1.0	0.0132	0.65	33,000
B5	300	1.0	0.0748	0.65	6000
B6	300	1.0	0.0367	0.56	17,000
B7	300	1.0	0.0367	0.85	5300

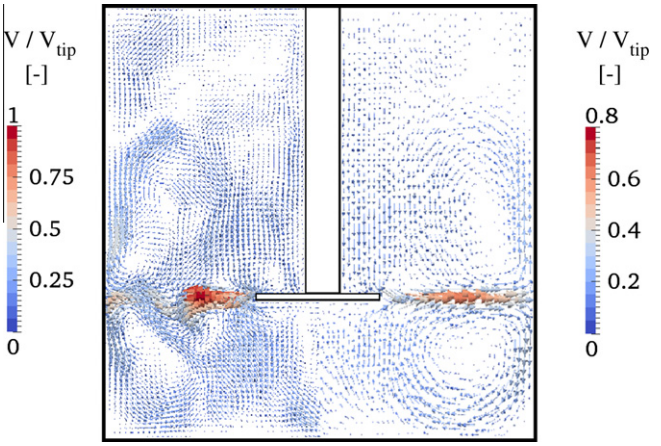

Fig. 1. Predicted instantaneous (left) and long-term averaged (right) velocity vector field in the mid-plane between the baffles (case A1).

For all simulations, a no-slip (wall) boundary condition was applied at all surfaces except for the top one, for which a free-slip boundary condition was employed to mimic a free surface flow. The reactor components were represented by sets of control points according to the immersed boundary condition. The diameter of the impeller was 30 times the size of a grid spacing. The distance between two control points at the impeller surface was $0.7h_\sigma$. The fluid domain was discretized by a uniform cubic grid of 88^3 lattices (except for some simulations in the grid sensitivity study), which corresponded to a grid spacing of 3.3×10^{-3} and 5×10^{-3} m in the single- and multiphase cases, respectively. The simulations began at a standstill and proceeded with a time step of 1.1×10^{-5} s for the single-phase simulations. In the multiphase cases, a liquid phase time step of 1.8×10^{-5} s and a sub-time step of 3.5×10^{-6} s for the calculation of the bubble motion were used. 30 impeller revolutions after startup from rest, information concerning the liquid phase and bubbles was collected over 30 and 60 impeller revolutions for the single- and multiphase simulations, respectively, and statistically processed.

The initial bubble diameter was assumed to be uniform at 8 mm in every case with aeration. This corresponded to a grid-spacing-to-bubble-diameter ratio h_σ/d_p of 0.625. Theoretically, the h_σ/d_p ratio should be larger than unity when the point-volume assumption is employed. Nevertheless, Sungkorn et al. (2011) demonstrated that this restriction could be relaxed, i.e., h_σ/d_p can be less than unity for a small number of bubbles present in the system. It should be greater than 0.5 for a small number of bubbles present in the system. Therefore, the size of bubbles was limited to 0.05–10 mm, corresponding to a h_σ/d_p range of 10–0.5. The number of bubbles tracked during simulations were in the order of O(10^4) in most cases.

All simulations were run in parallel, following the strategy introduced by Derksen and Van den Akker (1999) and Sungkorn et al. (2011). The wall-clock time for simulating of one impeller revolution in multiphase system was approximately 1.5 h when 4 Intel® Xeon® E5504 (at 2.0 GHz) processors were used.

4. Results and discussion

4.1. Single-phase stirred reactor

4.1.1. Flow hydrodynamics

Simulations were carried out following the settings of the A1 case in Table 2. The predicted instantaneous and long-term averaged liquid flow fields in the mid-plane between the baffles are shown in Fig. 1. A radial jet-like outflow with trailing vortices in the impeller plane can be observed, as it is expected for a Rushton disk turbine. The radial outflow significantly interacts with the tank wall inducing two recirculation loops in the region above and below the impeller level. Moreover, eddy-like structures could be observed in the bulk. Since the impeller was located close to the tank bottom, the lower recirculation loop interacted with the tank bottom and had a smaller size than the upper one. The upper recirculation loop was not strong enough to entirely agitate the liquid volume above the impeller, creating a stagnant zone (referred to as a region with relatively low liquid motion) near the liquid surface, i.e., above two-thirds of the reactor height. Similar flow structures could be observed in the long-term averaged flow field with a clearer identification of the stagnant zone in the region near the liquid surface. Note, that this flow structure should not be considered a cavern typically found in very viscous, highly shear-thinning liquids (with n value of 0.3 or less) (Venneker et al., 2010). Rather, these flow structures are caused by such factors as the position of the impeller, the (moderate) shear-thinning behavior of the liquid and the impeller Reynolds number Re$_r$ being in the transition regime.

In Fig. 2, the predicted axial and radial long-term averaged liquid velocity components are compared with the experimental data of Venneker (1999). The comparison was made in the plane of the baffle for the radial velocity profiles at various heights. Despite a coarse grid spacing employed during the simulation, the predicted flow field was in fair agreement with the experimental data, because the reactor had only a moderate impeller Reynolds number in this case (Re$_r$ = 2500) and the liquid exhibited only moderate shear-thinning behavior with n = 0.68. Additionally, the energy-containing eddies were at the scale corresponding to the impeller diameter. As such, most of the energy of the flow field was resolved during the simulation and the main features of the flow were accurately captured. A slightly over prediction of axial velocities near the top surface can be noticed. This is due to the fact that the free surface of the liquid is fixed with the computational domain by a free-slip boundary condition.

Fig. 3 (left) shows that the long-term averaged apparent liquid viscosity calculated using Eq. (1) varied within a small range. The lowest viscosity occurred in the impeller-swept region, under which the highest liquid deformation took place, and increased along the radial outflow. The highest viscosity was on the edge of the reactor and near the wall next to the upper recirculation loop, where almost no liquid motion was observed. The long-term averaged eddy viscosity is shown in Fig. 3 (right). As can be noticed, the

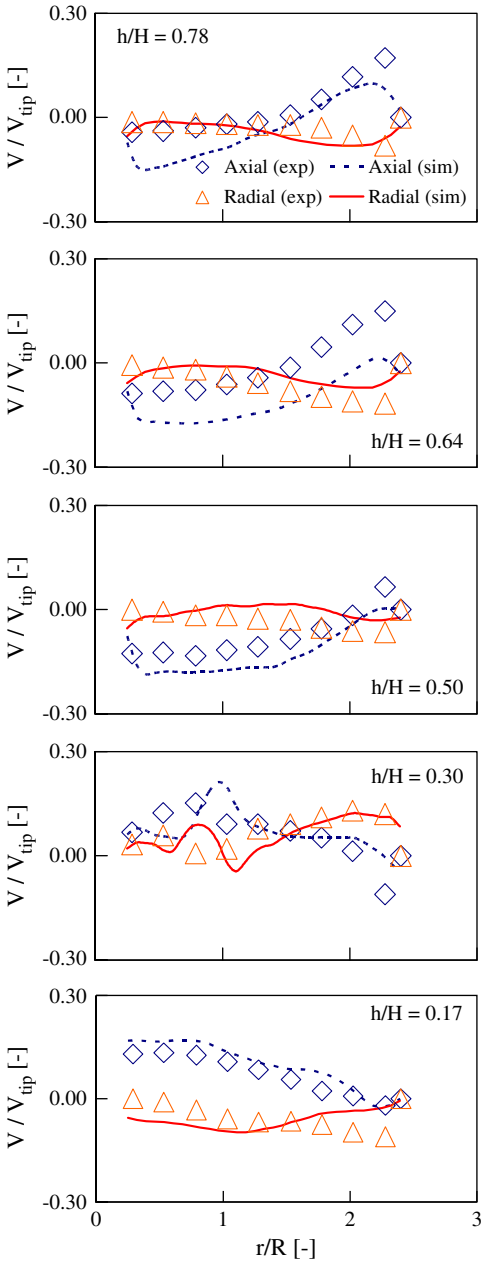

Fig. 2. Experimental and predicted (case A1) axial and radial long-term averaged velocity components in the baffle plane at various heights.

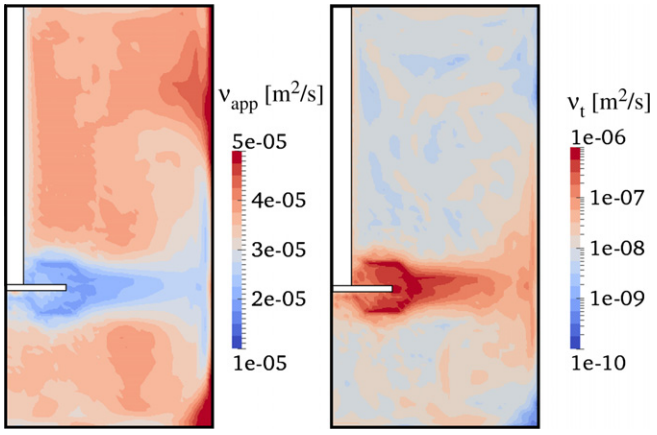

Fig. 3. Predicted long-term averaged apparent viscosity (left) and eddy viscosity (right) in the mid-plane between the baffles (case A1). Note that logarithmic scale is used for the eddy viscosity contour plot.

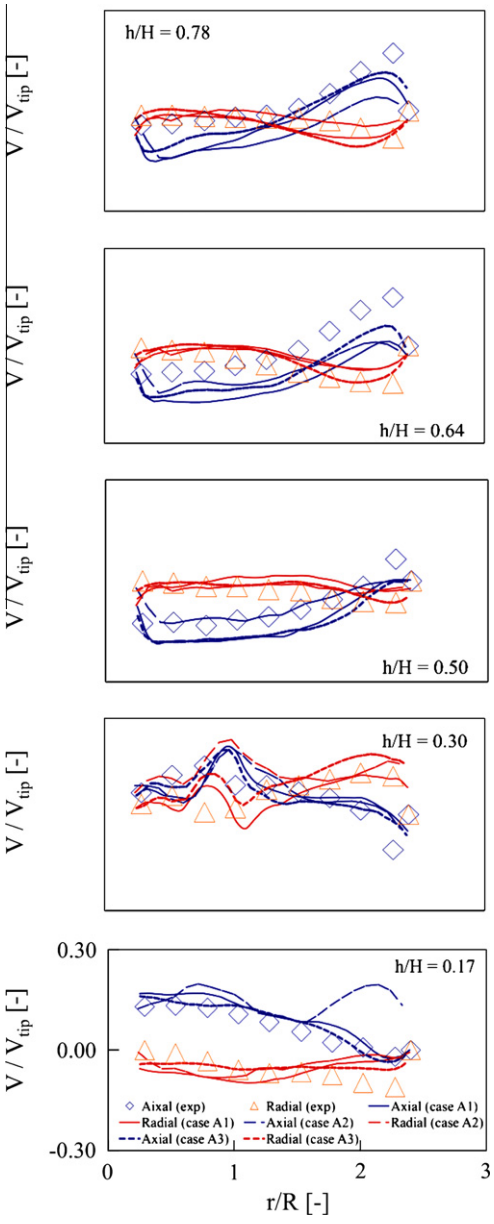

Fig. 4. Experimental and predicted (cases A1, A2 and A3) axial and radial long-term averaged velocity components in the baffle plane at various heights.

eddy viscosity shows the opposite trend from that observed for the apparent viscosity. The highest eddy viscosity occurred in the impeller-swept region due to the liquid motion induced by the impeller associating with the relatively low apparent viscosity in this region. Nevertheless, in this case in which the impeller Reynolds is relatively low anywhere in the tank, the magnitude of the eddy viscosity is more than one order of magnitude less than that of the apparent viscosity.

4.1.2. Grid sensitivity study

Effects of the grid resolution, i.e., of grid spacing, were studied by performing simulations with coarser (case A2 in Table 2) and finer grids (case A3). A comparison of the predicted axial and radial long-term averaged liquid velocity components with the experimental data is shown in Fig. 4. It can be observed that all simulations provide similar velocity profiles. The agreement that was

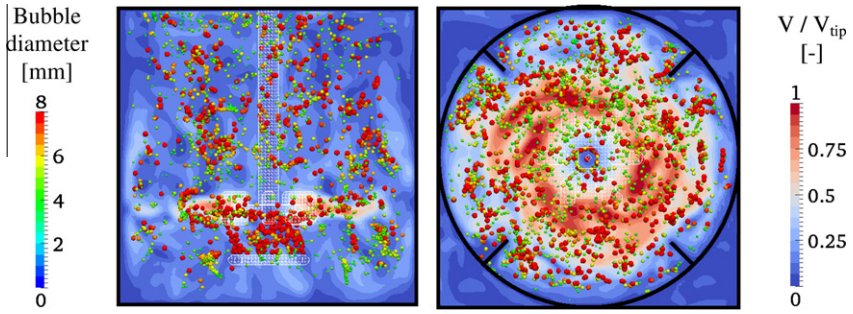

Fig. 5. Snapshot of bubble dispersion pattern and liquid velocity magnitude (case B1) in the mid-plane between the baffles (left) and a cross section at the impeller disc (right). Bubbles are highlighted and scaled by diameter. The snapshots were taken at the same moment.

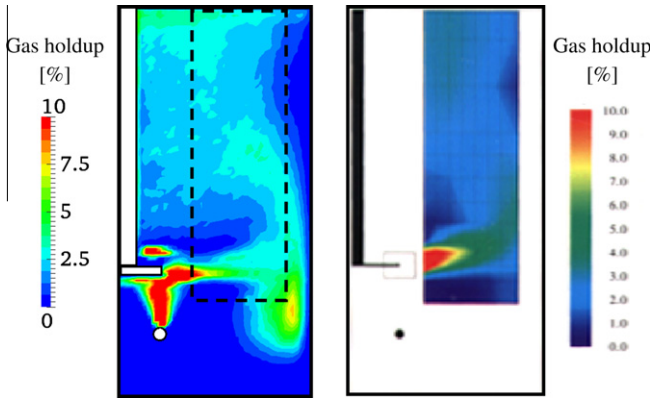

Fig. 6. Predicted (left) and experimental (right) long-term averaged local gas holdup (case B1).

achieved for the simulation with the finest grid spacing (case A3) was only a slightly better, which demonstrates a grid-independent behavior of the reactor simulation. However, in case A2 (coarse grid) significant deviations were found especially at larger radii. Thus, case A1 is deemed a sufficiently fine resolution of the flow at this Reynolds number.

Within the limitations of the Re_r value and shear-thinning behavior, the simulation results support the assumption proposed by Venneker (1999) that the SGS viscous stress in non-Newtonian liquids can be treated in a similar manner as it is in Newtonian liquids. However, in order to develop a predictive turbulence model for non-Newtonian liquids, detailed experimental data concerning a liquid flow field in a stirred reactor with a high Re_r value and various liquid rheologies are required.

In summary, we postulate that the presented modeling technique is a valid approximation. It was also shown that the choice of the grid spacing, which is restricted by the bubble diameter (as discussed earlier but not considered in the single-phase simulations), had only a marginal effect on the main features of the liquid flow field. Future studies should be focused on a further refinement of our modeling technique, e.g., a non-Newtonian turbulence model and a more sophisticated non-Newtonian liquid model.

4.2. Multiphase stirred reactor

4.2.1. Gas–liquid flow hydrodynamics

Simulations for aerated systems were carried out and parameters for the case B1 are summarized in Table 3. The resolution was identical to case A1. Bubbles were injected in the tank through the top surface of the ring sparger with a uniform initial diameter of 8 mm. Snapshot of the predicted bubble dispersion pattern and liquid velocity field in the mid-plane between the baffles is shown in Fig. 5. As in the single-phase stirred reactor, a radial jet-like outflow from the Rushton turbine can be observed in the vertical plane between the baffles. The flow velocity had the highest magnitude near the impeller blades and decreased in the radial direction towards the tank wall. The radial outflow induced two primary recirculation loops in the region above and below the impeller level. The influence of the sparger on the liquid flow field was also observed. Eddy-like structures were more pronounced in the bulk above the impeller than at the bottom, and near the liquid surface there was a stagnant zone. The temporal behavior of the liquid flow showed time-dependent flow structures. The bubbles fluctuated within a small range before they were drawn into the impeller-swept area. Most of the bubble breakup occurred in the impeller-swept area where small eddies reside. Small bubbles tended to follow the recirculation loop to the lower part of the reactor, while larger bubbles tended to rise as their buoyancy was strong enough to overcome the downwards liquid flow. In the volume above the impeller, some fraction of the bubbles was drawn into the upper recirculation loop resulting in a recycling into the upper impeller-swept region and, consequently, in a secondary breakup of the bubbles. Furthermore, the bubbles accumulated near the impeller's shaft due to the viscosity and the radial pressure gradient in the impeller's shaft region. Additionally, the downwards flow in that region prevented the bubbles from rising to the liquid surface.

Snapshot of the predicted bubble dispersion pattern and liquid velocity field at the cross section just below the impeller disc is shown in Fig. 5. In the view of this figure, the impeller rotates in counterclockwise direction. From the animated results (data available upon request), it can be observed that the wakes behind the impeller blades have velocity magnitudes that are slightly higher than the impeller tip speed. An interaction between the wakes and the baffles is also observed. Furthermore, the low pressure region behind the blades formed so-called ventilated cavities (Middleton and Smith, 2004): bubbles were drawn into the wakes behind the blades and subsequently dispersed horizontally. An accumulation of the bubbles near the impeller's shaft and on the windward side of the baffles can be seen on the snapshots.

The predicted and experimental long-term averaged gas holdup contour plots are shown in Fig. 6. The experimental data were measured with an optical fiber probe (Venneker, 1999) with the thickness of the measurement plane depending on the bubble size and the approaching angle of the bubble to the probe. A specific plane cannot be defined by such a measurement method. However, with a long enough averaging period, the phase-averaged procedure may be used for comparison the simulation. As can be seen, a qualitatively good agreement between our predictions and experimental results was achieved. A radial stream of gas bubbles

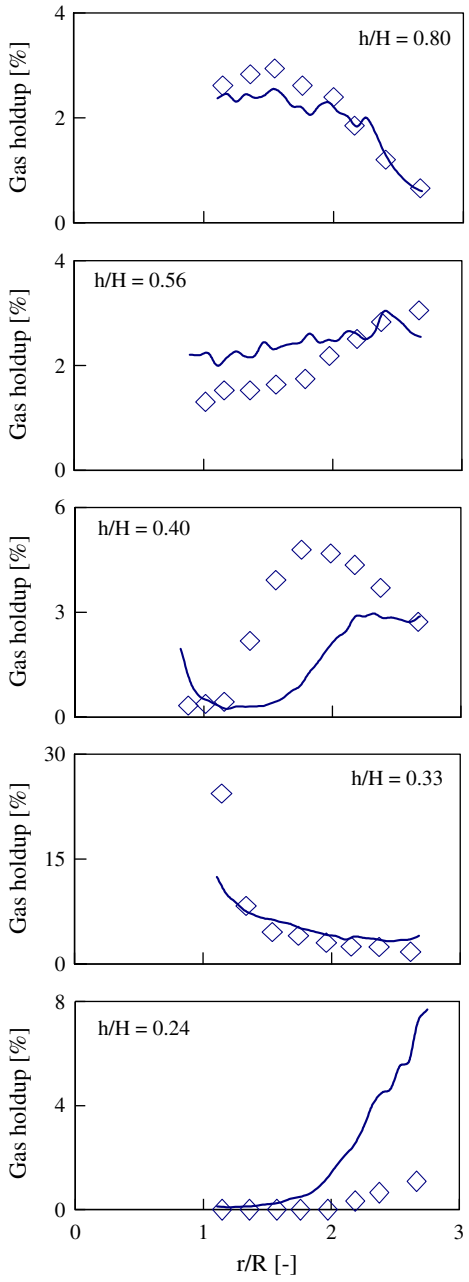

Fig. 7. Experimental and predicted (case B1) long-term averaged radial gas holdup profile at various heights.

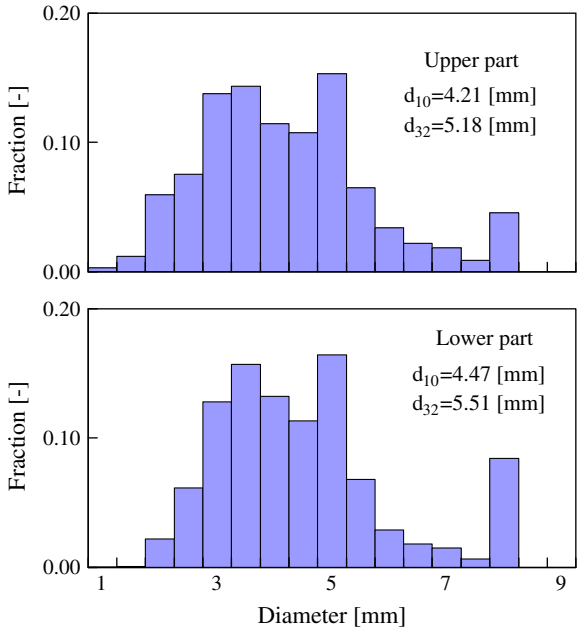

Fig. 8. Predicted long-term averaged bubble size distribution for case B1 in the entire volume above (top) and below the impeller disc (bottom).

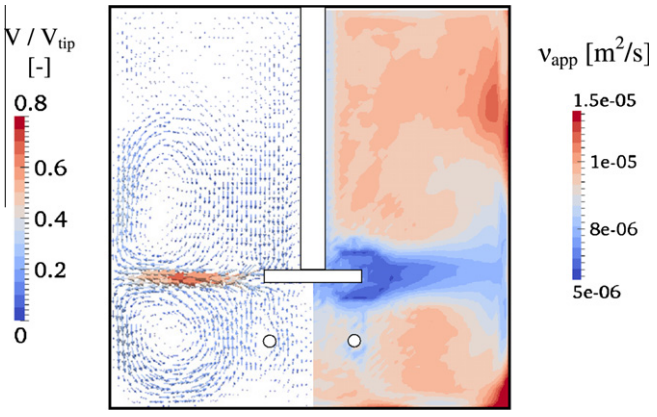

Fig. 9. Predicted long-term averaged liquid velocity (left) and apparent viscosity (right) in the mid-plane between the baffles (case B1).

towards the reactor wall was reproduced in the simulation, and the absence of significant gas holdup above and below the outflow stream was predicted. Moreover, the gas holdup near the wall towards the center axis at the liquid surface was correctly captured. Additionally, the simulation showed a high concentration of gas in the sparger's outflow, the impeller swept region and the region next to the impeller's shaft. Interestingly, a region of high concentration was also found above the impeller blades due to an equilibrium between the bubbles' buoyancy and the downward liquid flow resulting in a long bubble residence time. This behavior was also observed in our experiments (data available upon request).

Fig. 7 shows the predicted and experimental long-term averaged radial profile of the gas holdup at various heights. Again, a fairly good agreement between the simulation and experimental results was achieved. There were some deviations in the region right above and below the impeller, which could have been caused by factors such as the spherical bubble assumption, the lack of resolution to directly describe the interaction between the impeller and bubbles such as deforming and bouncing, a relatively coarse grid employed in the simulation, the lack of a reliable turbulence model for non-Newtonian liquids or also the inaccuracy of the intrusive measurement method. The latter unavoidably disturbs the flow field and may cause a significant deviation when the attack angle of the bubble is greater than 90°, as demonstrated by Bombac et al. (1997) for a conductivity-based probe.

The predicted long-term averaged bubble size distribution (BSD) in the region above and below the impeller is shown in Fig. 8. Both BSDs had a bimodal distribution with one mode having a diameter approximately half of the initial diameter and the other one having a diameter equal to the bubble's initial diameter. The lower part of the reactor had a slightly larger number mean diameter d_{10} and Sauter diameter d_{32} due to the presence of sparger in the lower part. Bubbles with a diameter larger than the initial

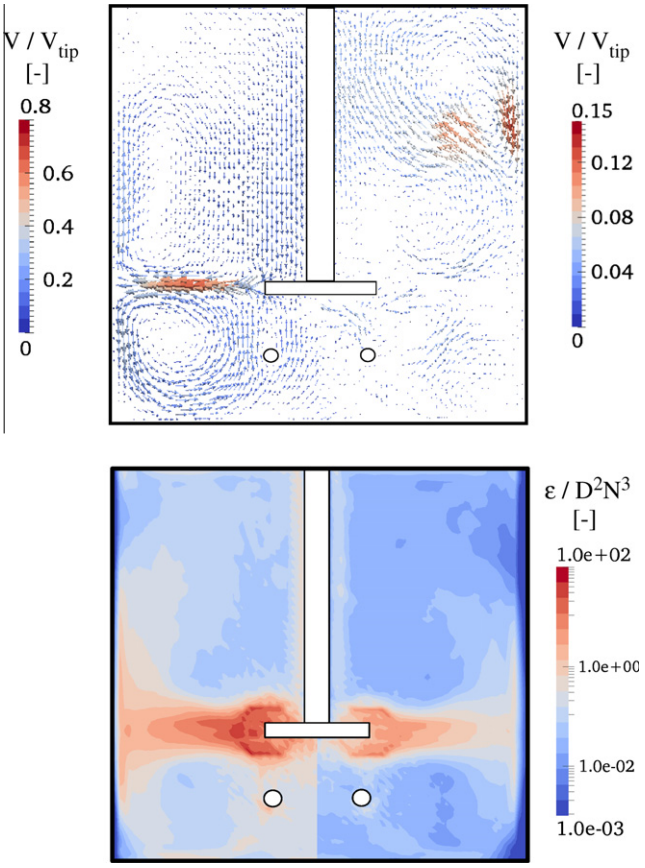

Fig. 10. (Top) predicted long-term averaged liquid velocity from simulation without aeration (case B2) (left) and the difference between liquid velocity for aerated (case B1) and unaerated condition (case B2) in the mid-plane between the baffles. (Bottom) predicted long-term averaged energy dissipation rate from simulation without aeration (case B2) (left) and with aeration (case B1) (right).

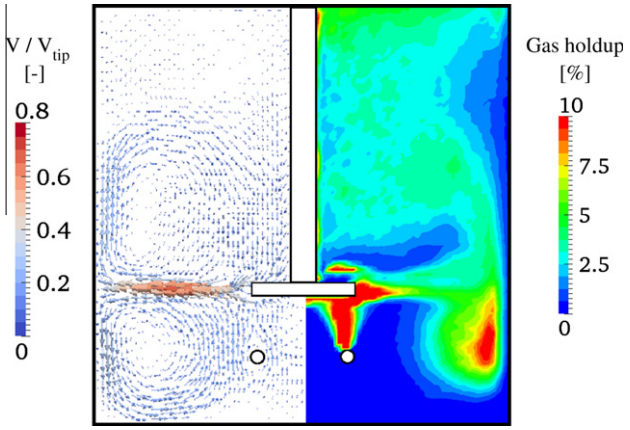

Fig. 11. Predicted long-term averaged liquid velocity (left) and gas holdup (right) in the mid-plane between the baffles from simulation case with a Newtonian liquid (case B3).

bubble size were rarely found, obviously because of the restriction of the maximum bubble size set in this work (i.e., only a coalescence of bubbles smaller than two times the grid spacing or a coalescence that would result in a bubble smaller than two times the grid spacing were allowed in the simulations). Hence, a bubble with a diameter of 8 mm, corresponding to 1.6 times the grid

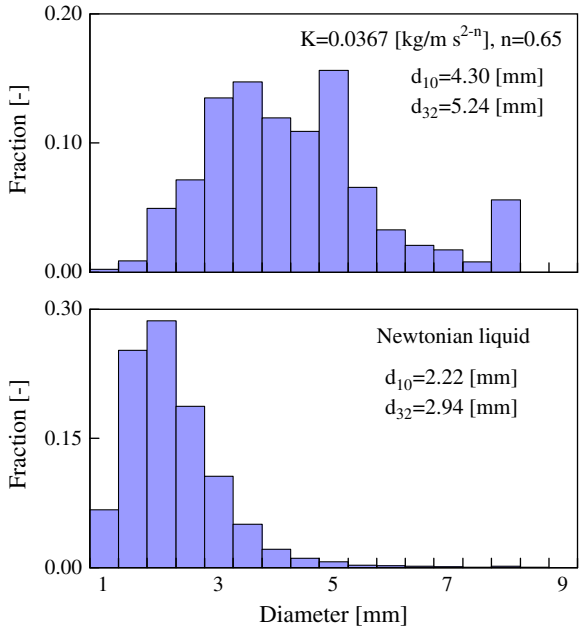

Fig. 12. Predicted long-term averaged bubble size distribution within the entire reactor from simulations with non-Newtonian (case B1) (top) and Newtonian liquids (case B3) (bottom).

spacing, would rarely coalesce. If the restriction were omitted, a smoother distribution around the larger mode would be obtained. However, it would only slightly affect the overall BSD.

The predicted long-term averaged liquid and apparent viscosities in the mid-plane between the baffles are shown in Fig. 9. The radial jet-like outflow induced by the Rushton turbine with two primary recirculation loops in the region above and below the impeller can be seen. Again, the radial outflow away from the impeller was not strong enough to create significant liquid motion near the surface, resulting in a stagnant zone near the liquid surface. The apparent viscosity showed a similar trend as in the single-phase simulation, with the lowest viscosity in the impeller-swept region and the highest viscosity in the lower corner of the reactor.

The effect of bubbles on the liquid flow field was determined by performing a simulation without aeration (case B2). The predicted long-term averaged liquid velocity from the case B2 and the difference between the liquid velocity, aerated (case B1) and unaerated (case B2), in the mid-plane between the baffles, are shown in Fig. 10 (top). Differences can be noticed in the upper part of the reactor, especially in the region near the wall. Bubbles at the impeller's blades reduce the pumping capacity of the impeller resulting in a weaker liquid stream and, consequently, in a weaker and smaller recirculation loop. The energy dissipation rate in the reactor under unaerated and aerated condition was also compared in Fig. 10 (bottom). The presence of bubbles significantly reduces the energy dissipation due to the strong coupling between phases.

4.2.2. Effects of liquid rheology

The effect of the non-Newtonian behavior was determined by comparing the simulation for a non-Newtonian liquid (case B1) with a simulation for a Newtonian liquid (case B3). Note that, in this work, we aimed at studying the effects of liquid rheology, therefore the impeller rotational speed and the gas flow rate were kept constant while liquid rheology was varied. The predicted long-term averaged liquid velocity and gas holdup in the mid-plane between the baffles for case B3 are displayed in Fig. 11 showing only a marginal difference in the liquid flow field between the

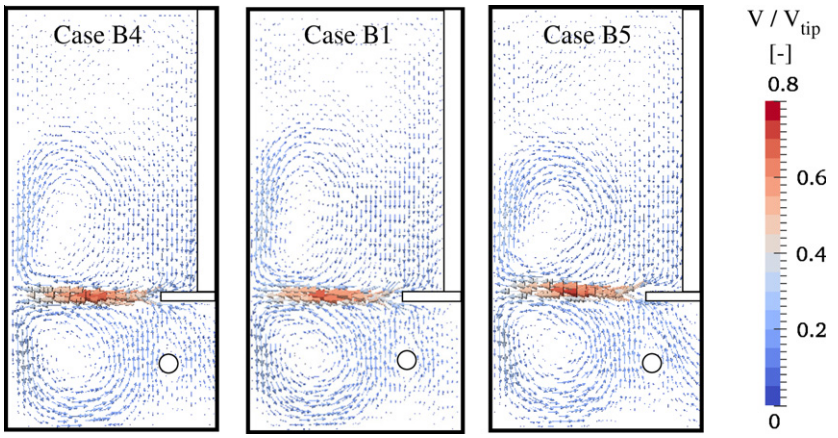

Fig. 13. Comparison of long-term averaged liquid velocity in the mid-plane between the baffles with increasing consistency coefficient from left to right (i.e., case B4, B1 and B5, respectively).

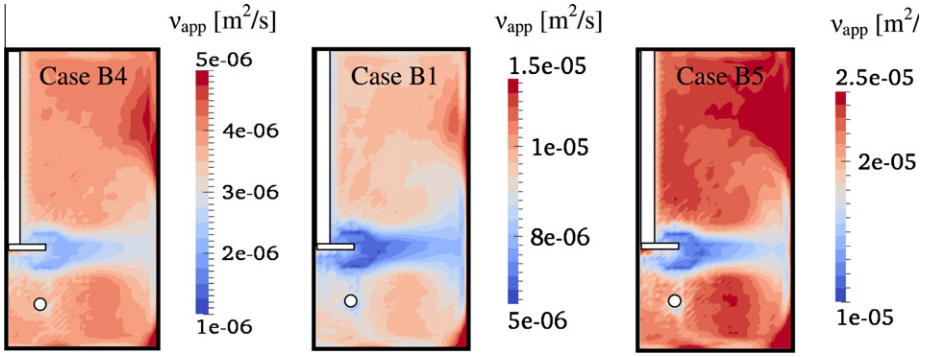

Fig. 14. Comparison of long-term averaged apparent viscosity in the mid-plane between the baffles with increasing consistency coefficient from left to right (i.e., case B4, B1 and B5, respectively).

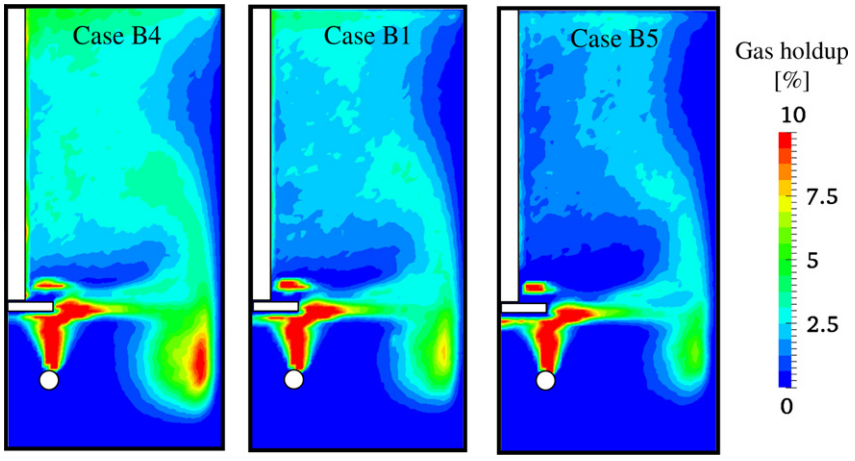

Fig. 15. Comparison of long-term averaged local gas holdup in the mid-plane between the baffles with increasing consistency coefficient from left to right (i.e., case B4, B1 and B5, respectively).

cases. In reality, this would result in a significant difference in power input. Nevertheless, in our work we focused only on the flow hydrodynamics. A significant difference could be observed when comparing the gas holdup distribution profiles. A higher gas concentration and larger dispersion area were obtained for a Newtonian liquid. The predicted long-term averaged BSDs in the reactor for both cases are shown in Fig. 12. The BSD had a bimodal distribution shape for a non-Newtonian liquid, while the BSD for a Newtonian liquid had a log-normal distribution shape. The value of d_{10} and d_{32} significantly decreased from 4.30 and 5.24 mm in the former case to 2.22 and 2.94 mm in the latter case. This is due to a higher Re_r value in the latter case which results in a higher turbulence intensity and, consequently, a greater amount of small eddies participating in the bubble breakage mechanism.

In the next case study, only the consistency coefficient was varied from 0.0367 kg/m s^{2-n} for case B1 to a lower value for case B4

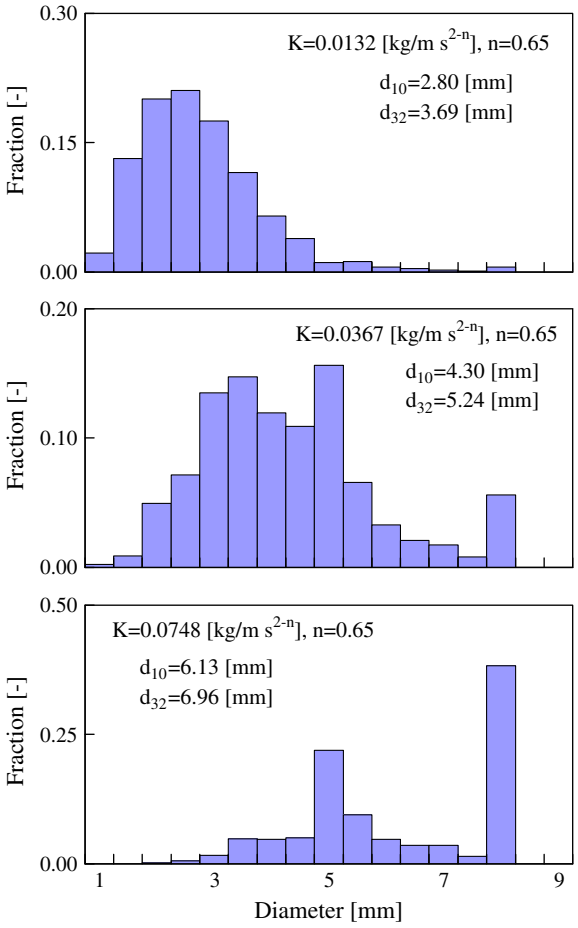

Fig. 16. Comparison of long-term averaged bubble size distribution within the entire reactor with increasing consistency coefficient from top to bottom (i.e., case B4, B1 and B5, respectively).

and a higher value for case B5. Correspondingly, the Re_r value changed from 12,000 for case B1 to 33,000 and 6000 for cases B4 and B5, respectively. Fig. 13 shows the predicted long-term averaged liquid velocity in the mid-plane between the baffles for the simulation cases described above. The Figure was arranged such that the consistency coefficient increases from left to right. As can be seen, the size of the upper recirculation changes with the consistency coefficient. The predicted long-term averaged apparent viscosity is shown in Fig. 14. For all simulations, the viscosity profile exhibited a similar trend, i.e., the lowest viscosity occurred in the impeller-swept region, increased along the outflow and had the minimum value on the edge of the reactor. However, as expected, the magnitude of the viscosity increased while the range of the viscosity decreased with the increased consistency coefficient. A significant difference in the gas holdup distribution was observed (Fig. 15). The increase in the consistency coefficient resulted in a lower concentration and a smaller dispersion area. The predicted BSD depicted in Fig. 16 shows that the decrease of the consistency coefficient from case B1 to case B4 led to a more pronounced bubble breakage, as can be noticed in the change of the BSD from a bimodal to a log-normal distribution with smaller d_{10} and d_{32} values. Additionally, an increase of the consistency coefficient led to a lower bubble breakage, as the bimodal distribution shape obtained for case B5 demonstrates.

We also studied the effects of the power-law index n in shear-thinning liquids. The value of n was varied from 0.65 in case B1 to 0.56 and 0.85 in cases B6 and B7, respectively. A decrease in n value implies that the liquid exhibits higher shear-thinning behavior. Accordingly, the Re_r value changed from 12,000 in case B1 to 17,000 and 5300 in cases B6 and B7, respectively. Plots of the long-term averaged liquid velocity are shown in Fig. 17. It can be observed that the shape and size of the upper recirculation differ slightly between the cases. Venneker et al. (2010) measured liquid velocity components at the level of the impeller disc in a single-phase stirred reactor with shear-thinning fluids and concluded that the values of Re_r and n had no effect on the measured mean radial and tangential velocity components. Only the axial velocity component depended on the Re_r value. As stated in the previous Section, the presence of bubbles for the range of aeration rate considered in this study only had a marginal effect on the liquid flow field. Plots of the predicted long-term averaged apparent viscosity in Fig. 18 show that an increase in n value resulted in an increase in the viscosity and a decrease in the viscosity range. The trend for the viscosity was qualitatively similar for all cases. The difference between the viscosity in the impeller-swept region and the bulk was decreased at a higher n value. The predicted long-term averaged gas holdup is depicted in Fig. 19. It can be clearly seen that the concentration and dispersion areas decreased with the increase of n value. In the case B7, bubbles rarely disperse in the reactor, and most of them rise towards the liquid surface. The predicted long-term averaged BSD in the reactor is shown in Fig. 20. The d_{10} and d_{32} values increase with the increased n value. Significant differences were observed between cases B1 and B7: BSD for case B7 shows that almost no breakup occurred in the

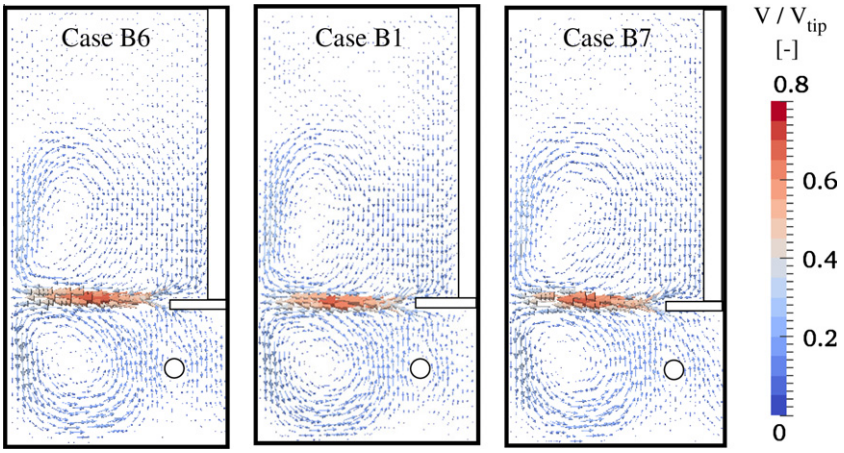

Fig. 17. Comparison of long-term averaged liquid velocity in the mid-plane between the baffles with increasing power-law index from left to right (i.e., case B6, B1 and B7, respectively).

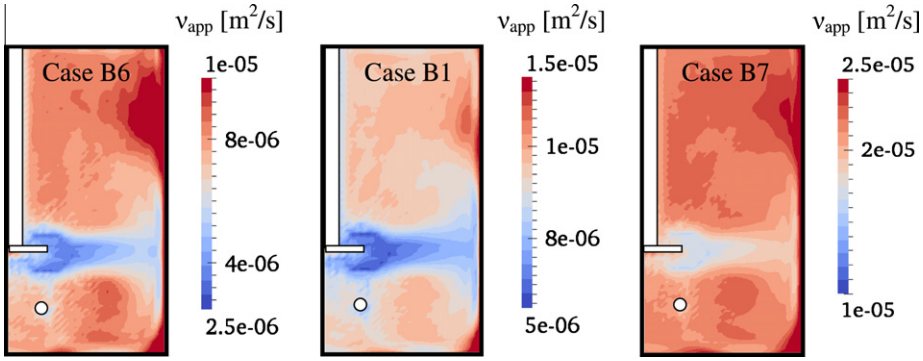

Fig. 18. Comparison of the long-term averaged apparent viscosity in the mid-plane between the baffles to increased power-law index from left to right (i.e., case B6, B1 and B7, respectively).

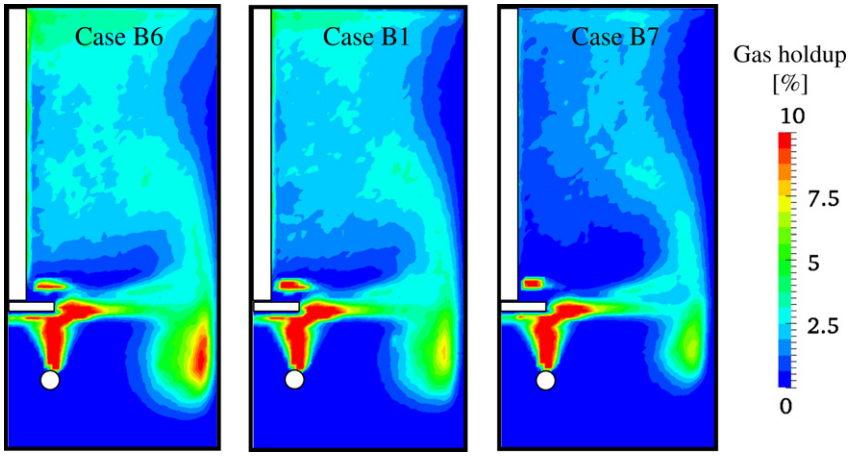

Fig. 19. Comparison of the long-term averaged local gas holdup in the mid-plane between the baffles to the increased power-law index from left to right (i.e., case B6, B1 and B7, respectively).

reactor resulting in high values of d_{10} and d_{32}. Thus, the n-value has the most significant impact on the bubble size distribution. This result is very interesting, especially for practical applications. For instance, in some situations, a Newtonian liquid would disperse bubbles while shear-thinning liquid does.

5. Conclusions

In this study, we expanded our previous work (Derksen, 2003; Sungkorn et al., 2011, 2012; Derksen and Van den Akker, 1999) to develop a modeling technique for simulations of aerated stirred reactors with shear-thinning power law liquids. The proposed model accounted for the bubble breakup and coalescence, and the non-Newtonian behavior was modeled using a truncated power-law model (Gabbanelli et al., 2005). A variation of the LB scheme of Somers (1993) was used to discretize the filtered conservation equations of the liquid phase. A bubble cluster concept was employed with a point-volume assumption to track the bubble motion. The drag force was calculated using the correlation derived from experiments with pseudoplastic liquids (Dewsbury et al., 1999). The collision, coalescence and breakup of the bubbles were treated as stochastic events. The IBC by Derksen et al. (1997) was applied to describe the effect of the moving reactor components on the liquid phase and on the bubbles.

The comparison between the predicted and experimental liquid flow fields of a single-phase stirred reactor with a shear-thinning power law liquid showed that the simulation can capture the main features of the flow field. A grid sensitivity study suggested that finer grids provided only a slightly better prediction. It was also found that a coarser grid captured most of the main flow features, e.g., a radial outflow and recirculation loops above and below the impeller. The study was performed with a moderate impeller Reynolds number, i.e., $Re_r = 2500$. Hence, the validity range was justified within the limitations of Re_r and liquid rheology. In order to further justify the validity and develop a reliable modeling technique, detailed experimental data of a stirred reactor with high Re_r and a variety of liquid rheologies are required. However, we assumed that our modeling technique was sufficiently valid for the simulations carried out in this work, at least with regard to capturing the main flow features. Further works (both experimentally and numerically) on modeling of non-Newtonian turbulence model, and closures for the dispersed bubble phase are required to accurately capture all features within aerated stirred reactors.

When the predicted gas holdup of an aerated stirred reactor with a shear-thinning power law liquid was compared to the experimental data of Venneker et al. (2002), a qualitatively fair agreement was achieved. It was numerically demonstrated that the presence of bubbles, within the aeration rate employed in this work, had an effect mainly on the liquid flow field in the upper part of the reactor and especially near the wall. This demonstrates the feasibility of using the EL approach with the stochastic model for numerical modeling of aerated stirred reactors. Nevertheless, detailed information concerning gas and liquid phase in a stirred

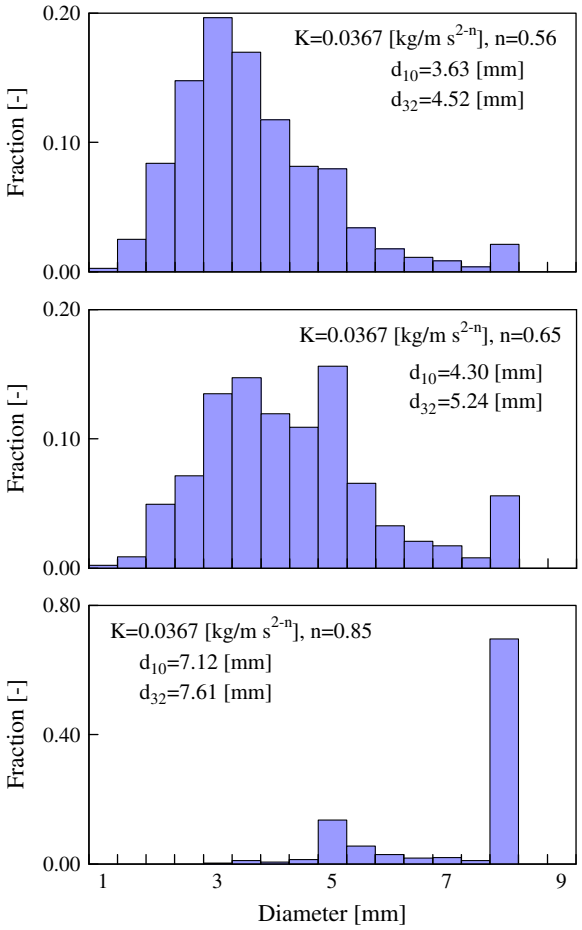

Fig. 20. Comparison of the long-term averaged bubble size distribution within the entire reactor to the increased power-law index from top to bottom (i.e., case B6, B1, and B7, respectively).

reactor (and a bubble column) with non-Newtonian liquid is necessary for deriving and validation of closures for the gas phase.

Furthermore, the presented modeling technique was used to study the effect of liquid rheology on the flow hydrodynamics, the bubble dispersion pattern and BSD. It was found that the increase in the consistency coefficient (i.e., viscosity) and the power-law index (i.e., shear-thinning behavior) resulted in the decrease in the concentration and dispersion areas of the bubbles. Accordingly, the BSD changed significantly from bimodal to log-normal distribution shape in some cases. It is known that the change in the liquid rheology resulted in the change of the Re_r value and, consequently, in the turbulence intensity, the size of eddies and the viscosity distribution within the reactor. As such, these factors affect the breakage of the bubbles, as well as their rise velocity and dispersion pattern. It is not yet clear if the dispersion pattern and BSD only depend on the Re_r value or if they interact with the liquid rheology and Re_r value in a more complex way. In the future we plan to study the subject both numerically and experimentally to gain more understanding.

Some of the assumptions employed in this work were conjectural. However, from an engineering point of view, they are sufficient to gain a preliminary understanding of the phenomena within a complex aerated stirred reactor with pseudoplastic liquids. Since the presented modeling technique utilizes elementary physical principles, it can be considered an alternative engineering tool to gain valuable information of complex industrial-scale reactors.

Acknowledgements

This work was partially funded by Sandoz GmbH, Kundl, Austria and the Research Center Pharmaceutical Engineering, Graz, Austria. Further details of the gas-liquid flow in the reactor and animated results of the dispersion pattern and the liquid velocity field are available upon request.

References

Arlov, D., Revstedt, J., Fuchs, L., 2008. Numerical simulation of gas-liquid Rushton stirred reactor – LES and LPT. Comput. Fluids 37, 793–801.
Bakker, A., Van den Akker, H.E.A., 1994. A computational model for the gas-liquid flow in stirred reactors. Trans. Inst. Chem. Eng. 72, 594–606.
Bird, R.B., Stewart, W.E., Lightfoot, E.N., 2007. Transport Phenomena, second ed. John Wiley & Sons, New York.
Bombac, A., Zun, I., Filipic, B., Zumer, M., 1997. Gas-filled cavity structures and local void fraction distribution in aerated stirred vessel. AIChE J. 43, 2921–2931.
Chesters, A.K., 1975. The applicability of dynamic-similarity criteria to isothermal, liquid-gas, two-phase flows without mass transfer. Int. J. Multiphase Flow. 2, 191–212.
Chesters, A.K., 1991. The modeling of coalescence processes in fluid-liquid dispersions: a review of current understanding. Trans. Inst. Chem. Eng. 69, 259–270.
Deen, N.G., Solberg, T., Hjertager, B.H., 2002. Flow generated by an aerated Rushton impeller: two-phase PIV experiments and numerical simulations. Can. J. Chem. Eng. 80, 1–15.
Deen, N.G., Van Sint Annaland, M., Kuipers, J.A.M., 2004. Multi-scale modeling of dispersed gas-liquid two-phase flow. Chem. Eng. Sci. 59, 1853–1861.
Derksen, J.J., 2003. Numerical simulation of solids suspension in a stirred tank. AIChE J. 49, 2700–2714.
Derksen, J.J., Kooman, J.L., Van den Akker, H.E.A., 1997. Parallel fluid flow simulation by means of a lattice-Boltzmann scheme. Lect. Notes Comput. Sci. 125, 524–530.
Derksen, J.J., Van den Akker, H.E.A., 1999. Large eddy simulation on the flow driven by a Rushton turbine. AIChE J. 45, 209–221.
Dewsbury, K., Karamanev, D., Margaritis, A., 1999. Hydrodynamic characteristics of free rise of light solid particles and gas bubbles in non-Newtonian liquids. Chem. Eng. Sci. 54, 4825–4830.
Eggels, J.G.M., Somers, J.A., 1995. Numerical simulations of free convective flow using the lattice-Boltzmann scheme. Int. J. Heat Fluid Flow. 16, 357–364.
Gabbanelli, S., Drazer, G., Koplik, J., 2005. Lattice Boltzmann method for non-Newtonian (power-law) fluids. Phys. Rev. E. 72, 046312.
Gogate, P.R., Beenackers, A.A.C.M., Pandit, A.B., 2000. Multiple-impeller systems with a special emphasis on bioreactor: a critical review. Biochem. Eng. J. 6, 109–144.
Goldstein, D., Handler, R., Sirovich, L., 1993. Modeling a no-slip flow boundary with an external force field. J. Comput. Phys. 105, 354–366.
Grenville, R.K., Nienow, A.W., 2004. Blending of miscible liquids. In: Paul, E.L., Atiemo-Obeng, V.A., Kresta, S.M. (Eds.), Handbook of Industrial Mixing: Science and Practice. Wiley, New York, pp. 507–542.
Hartmann, H., Derksen, J.J., Montavon, C., Pearson, J., Hamill, I.S., Van den Akker, H.E.A., 2004. Assessment of large eddy and RANS stirred tank simulations by means of LDA. Chem. Eng. Sci. 59, 2419–2432.
Hemrajani, R.R., Tatterson, G.B., 2004. Mechanically stirred vessels. In: Paul, E.L., Atiemo-Obeng, V.A., Kresta, S.M. (Eds.), Handbook of Industrial Mixing: Science and Practice. Wiley, New York, pp. 345–390.
Hu, G., Celik, I., 2008. Eulerian-Lagrangian based large-eddy simulation of a partially aerated flat bubble column. Chem. Eng. Sci. 63, 253–271.
Lane, G.L., Schwarz, M.P., Evans, G.M., 2005. Numerical modelling of gas-liquid flow in stirred tanks. Chem. Eng. Sci. 60, 2203–2214.
Luo, H., Svendsen, H.F., 1996. Theoretical model for drop and bubble breakup in turbulent dispersions. AIChE J. 42, 1225–1233.
Metzner, A.B., Otto, R.E., 1957. Agitation of non-Newtonian fluids. AIChE J. 3, 3–10.
Middleton, J.C., Smith, J.M., 2004. Gas-liquid mixing in turbulent systems. In: Paul, E.L., Atiemo-Obeng, V.A., Kresta, S.M. (Eds.), Handbook of Industrial Mixing: Science and Practice. Wiley, New York, pp. 585–638.
Moilanen, P., Laakkonen, M., Aittamaa, J., 2006. Modeling aerated fermenters with computational fluid dynamics. Ind. Eng. Chem. Res. 45, 8656–8663.
Moilanen, P., Laakkonen, M., Visuri, O., Aittamaa, J., 2007. Modeling local gas-liquid mass transfer in agitated viscous shear-thinning dispersions with CFD. Ind. Eng. Chem. Res. 46, 7289–7299.
Montante, G., Horn, D., Paglianti, A., 2008. Gas-liquid flow and bubble size distribution in stirred tanks. Chem. Eng. Sci. 63, 2107–2118.
Montante, G., Paglianti, A., Magelli, F., 2007. Experimental analysis and computational modelling of gas-liquid stirred vessels. Trans. IChemE. 85, 647–653.
Murthy, B.N., Joshi, J.B., 2008. Assessment of standard k-ε, RSM and LES turbulence models in a baffled stirred vessel agitated by various impeller designs. Chem. Eng. Sci. 63, 5468–5495.
Ranade, V.V., Van den Akker, H.E.A., 1994. A Computational snapshot of gas-liquid flow in based stirred reactors. Chem. Eng. Sci. 49, 5175–5192.

Smagorinsky, J., 1963. General circulation experiments with the primitive equations: 1. The basic experiment. Mon. Weather. Rev. 91, 99–164.
Somers, J.A., 1993. Direct simulation of fluid flow with cellular automata and the lattice-Boltzmann equation. J. Appl. Sci. Res. 51, 127–133.
Sommerfeld, M., 2001. Validation of a stochastic Lagrangian modeling approach for inter-particle collisions in homogeneous isotropic turbulence. Int. J. Multiphase Flow. 27, 1829–1858.
Sommerfeld, M., Bourloutski, E., Broeder, D., 2003. Euler/Lagrange calculations of bubbly flows with consideration of bubble coalescence. Can. J. Chem. Eng. 81, 508–518.
Sommerfeld, M., Decker, S., 2004. State of the art and future trends in CFD simulation of stirred vessel hydrodynamics. Chem. Eng. Technol. 27, 215–224.
Sommerfeld, M., Kohnen, G., Rueger, M., 1993. Some open questions and inconsistencies of Lagrangian particle dispersion models. In: Proceedings of the Ninth Symposium on Turbulent Shear Flows, Kyoto, Japan.
Sungkorn, R., Derksen, J.J., Khinast, J.G., 2012. Euler–Lagrange modeling of a gas–liquid stirred ractor with consideration of bubble breakage and coalescence. AIChE J. 58, 1356–1370.
Sungkorn, R., Derksen, J.J., Khinast, J.G., 2011. Modeling of turbulent gas-liquid bubbly flows using stochastic Lagrangian model and lattice-Boltzmann scheme. Chem. Eng. Sci. 66, 2745–2757.
Venneker, B.C.H., 1999. Turbulent non-Newtonian Fluid Flow and Gas Dispersion in Stirred Vessels, Ph.D. Thesis. University of Delft, The Netherlands.
Venneker, B.C.H., Derksen, J.J., Van den Akker, H.E.A., 2002. Population balance modeling of aerated stirred vessels based on CFD. AIChE J. 48, 673–685.
Venneker, B.C.H., Derksen, J.J., Van den Akker, H.E.A., 2010. Turbulent flow of shear-thinning liquids in stirred tanks – the effects of Reynolds number and flow index. Chem. Eng. Res. Des. 88, 827–843.
Zhang, Y., Yang, C., Mao, Z.-S., 2008. Large eddy simulation of the gas-liquid flow in a stirred tank. AIChE J. 54, 1963–1974.